Janus Pyrrolopyrrole Aza-dipyrrin: Hydrogen-Bonded Assemblies and Slow Magnetic Relaxation of the Cobalt(II) Complex in the Solid State

Ishizaki, Toshiharu
Department of Chemistry Graduate School of Science Osaka University

Karasaki, Hideaki
Department of Chemistry and Biochemistry Graduate School of Engineering, Kyushu University

Kage, Yuto
Department of Chemistry and Biochemistry Graduate School of Engineering, Kyushu University

Kamioka, Misaki
Department of Chemistry and Biochemistry Graduate School of Engineering, Kyushu University

他

出版情報：Chemistry - A European Journal. 27 (49), pp.12686-12692, 2021-09-01. Wiley
バージョン：

FULL PAPER

Janus Pyrrolopyrrole aza-Dipyrrin: Hydrogen-Bonded Assemblies and Slow Magnetic Relaxation of the Cobalt(II) Complex in the Solid State

Toshiharu Ishizaki[+,†],[a] Hideaki Karasaki[+],[b] Yuto Kage,[b] Misaki Kamioka,[b] Yitong Wang,[b] Shigeki Mori,[c] Naoto Ishikawa,[a] Takamitsu Fukuda,*[a] Hiroyuki Furuta,*[b] and Soji Shimizu*[b]

[a] *Dr. T. Ishizaki, Prof. Dr. N. Ishikawa, Prof. Dr. T. Fukuda*
Department of Chemistry, Graduate School of Science
Osaka University
Toyonaka 560-0043 (Japan)
E-mail: tfukuda@chem.sci.osaka-u.ac.jp

[b] *H. Karasaki, Dr. Y. Kage, M. Kamioka, Y. Wang, Prof. Dr. H. Furuta, Prof. Dr. S. Shimizu*
Department of Chemistry and Biochemistry, Graduate School of Engineering and Center for Molecular Systems (CMS)
Kyushu University
Fukuoka 819-0395 (Japan)
E-mail: hfuruta@cstf.kyushu-u.ac.jp, ssoji@cstf.kyushu-u.ac.jp

[c] *Dr. S. Mori*
Advanced Research Support Center (ADRES)
Ehime University
Matsuyama 790-8577 (Japan)

[+] *These authors contributed equally to this work.*

[†] *Current address: Department of Chemistry, College of Humanities and Sciences*
Nihon University, Tokyo 156-8550 (Japan)

Supporting information for this article is given via a link at the end of the document.

Abstract: A novel pyrrolopyrrole azadipyrrin (**Janus-PPAD**) with Janus duality was synthesized by a Schiff base forming reaction of diketopyrrolopyrrole. The orthogonal interactions of the hydrogen-bonding ketopyrrole and metal-coordinating azadipyrrin moieties in **Janus-PPAD** enabled arrangement of metal ions at regular intervals: zinc(II) and cobalt(II) coordination provided metal-coordinated **Janus-PPAD** dimers, which can subsequently form hydrogen-bonded one-dimensional arrays both in solution and in the solid state. The supramolecular assembly formation of the zinc(II) complex in solution was investigated by ^{1}H NMR spectroscopy based on the isodesmic model, in which a binding constant for the elongation of assemblies is constant. In the solid state, owing to the tetrahedral coordination, the cobalt(II) complex exhibited a slow magnetic relaxation due to the negative D value of −27.1 cm^{-1} with the effective relaxation energy barrier U_{eff} of 38.0 cm^{-1}. The effect of magnetic dilution on the relaxation behavior is discussed. The relaxation mechanism in the low temperature range was analyzed by considering spin lattice interactions and quantum tunneling effects. The easy-axis magnetic anisotropy was confirmed, and the relevant wave functions were obtained by *ab initio* CASSCF calculations.

Introduction

Diketopyrrolopyrrole (DPP)[1,2] has been widely used in industry as a red pigment owing to its photo and thermal stabilities and low solubility (Figure 1). Recent upsurge of application studies of DPP in the fields of imaging probes, light-mediated therapies,[3] and organic electronics, such as organic photovoltaics (OPVs),[4,5] organic field effect transistors (OFETs),[6] and organic light emitting diodes (OLEDs),[7] has been triggered by the synthesis of *N*-alkylated DPP derivatives with sufficient solubility to organic solvents. To enhance the optical properties of DPP toward respective applications, extension of the π-conjugation at 1,3,4, and 6-positions has also been intensively investigated.[8–10]

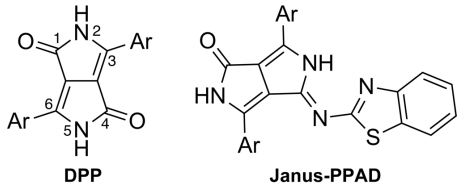

Figure 1. Structures of DPP (left) with atom numbering and **Janus-PPAD** (right).

The robust pigmentary character of DPP results from self-complementary hydrogen bond formation of the ketopyrrole moieties and strong π-π stacking interactions. Despite the significant interest in the hydrogen-bonding capability of DPP in terms of supramolecular chemistry to create complex architectures, this functionality has rarely been implemented into the DPP-based functional molecular designs because the hydrogen-bonding NH groups are replaced with solubilizing *N*-alkyl groups in most cases. During the synthesis of π-extended DPP derivatives called pyrrolopyrrole aza-BODIPYs (PPABs) in our previous study,[10] we noticed that a Schiff base forming reaction of DPP using one equivalent of azaarylamine converted one ketopyrrole moiety to an azadipyrrin structure, whereas the other ketopyrrole moiety remained intact. Because of the Janus duality of the hydrogen-bonding ketopyrrole moiety and the metal-coordinating azadipyrrin moiety, this DPP–azadipyrrin hybrid named Janus pyrrolopyrrole azadipyrrin (**Janus-PPAD**, Figure 1) can form one-dimensional supramolecular assemblies. In this study, we examined cobalt(II) and zinc(II) complexation of **Janus-PPAD**, which resulted in the formation of hydrogen-bonded one-

dimensional arrays of metal-coordinated dimers (**Janus-PPAD-Co** and **Janus-PPAD-Zn**) in the solid state. The hydrogen-bonding capability of **Janus-PPAD-Zn** was also investigated in solution by ^{1}H NMR and diffusion-ordered NMR (DOSY) spectroscopy and compared with reference compounds, which can only form either a hydrogen-bonded dimer or a metal-coordinated dimer. Owing to the tetrahedral coordination of the central cobalt(II) ion, **Janus-PPAD-Co** exhibits single-molecule magnet (SMM) behaviors in the solid state. The dynamic magnetic properties and the effect of the intermolecular hydrogen bonds on the magnetic properties were investigated by alternative current (ac) magnetic susceptibility measurements on **Janus-PPAD-Co** and its magnetically diluted sample prepared by mixing **Janus-PPAD-Co** and **Janus-PPAD-Zn**.

Results and Discussion

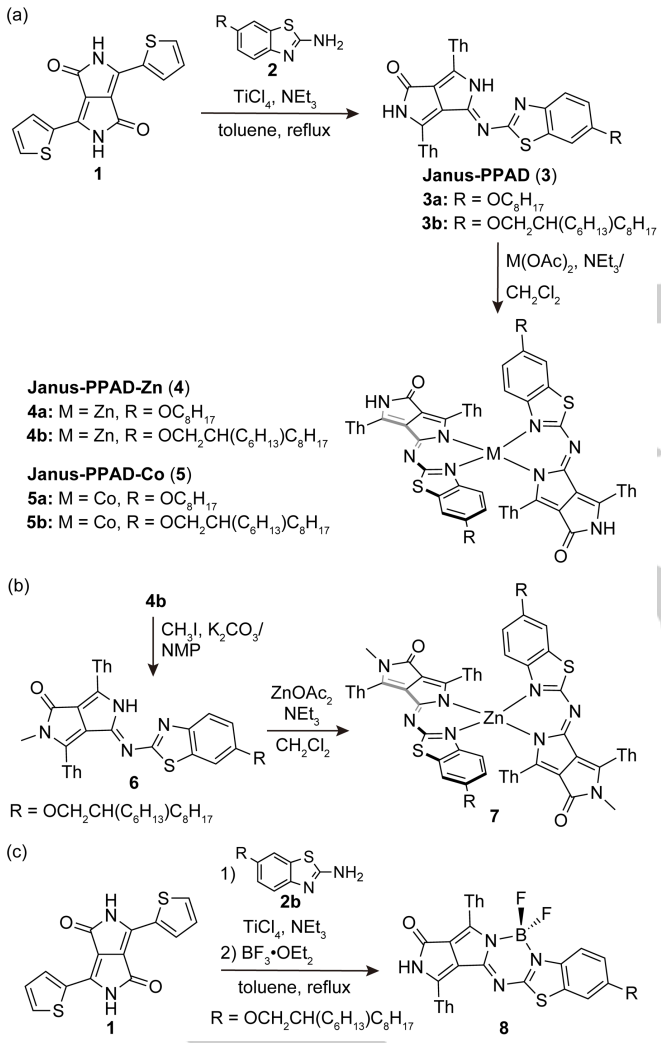

Scheme 1. Synthesis of (a) **Janus-PPAD** (**3**) and its metal complexes (**4** and **5**) and (b,c) reference compounds (**6**, **7**, and **8**) with either a metal-coordinating or a hydrogen-bonding capability. Th represents a 2-thienyl group.

Janus-PPAD was synthesized under the Schiff base forming reaction conditions, which were modified from those of the pyrrolopyrrole aza-BODIPY (**PPAB**) synthesis in our previous study.[10] To convert one ketopyrrole moiety into an azadipyrrin structure, one equimolar amount of 6-alkoxy-substituted 2-aminobenzothiazole **2** was reacted with DPP bearing 2-thienyl substituents (**1**) under mild reaction conditions using 0.5 equiv of titanium tetrachloride ($TiCl_4$) and 2.0 equiv of triethylamine. After purification by silica gel column chromatography and recrystallization, **Janus-PPAD** (**3**) was obtained in 31–49% yields (Scheme 1). **Janus-PPAD** was reacted with metal salts (cobalt(II) acetate dihydrate and zinc(II) acetate dihydrate) to provide metal-coordinated dimers (**Janus-PPAD-Zn** (**4**) and **Janus-PPAD-Co** (**5**)) in moderate yields. Relatively lower yields of the octyloxy-substituted compounds (**4a** and **5a**) than those of 2-hexyldecyloxy-substituted ones (**4b** and **5b**) are ascribed to the low solubility of ligand **3a**. As reference compounds, DPP–azadipyrrin hybrids with either a metal-coordinating or a hydrogen-bonding capability (**6**, **7**, and **8**) were also synthesized. All compounds were characterized by high-resolution mass spectrometry, ^{1}H NMR spectroscopy, and single crystal X-ray diffraction analysis (Figures 2 and S1–S7).[11] For solution studies, such as ^{1}H NMR, DOSY, and UV/vis absorption spectroscopic studies, compounds bearing 2-hexyldecyloxy substituents (**3b–5b**) were used, whereas magnetic studies were performed on the zinc and cobalt complexes with octyloxy substituents (**4a** and **5a**).

As shown in Figure 2, **Janus-PPAD-Zn** and **Janus-PPAD-Co** possess metal-centered chirality due to the tetrahedral coordination of asymmetric **Janus-PPAD** ligands. In the crystal packing diagram, Δ and Λ enantiomers are alternately bound to form one-dimensional arrays by the self-complementary hydrogen bonds between the ketopyrrole moieties with NH···O distances of 1.913 Å for **4a** and 1.939 Å for **5a** (Figures 2c and S8–S9).

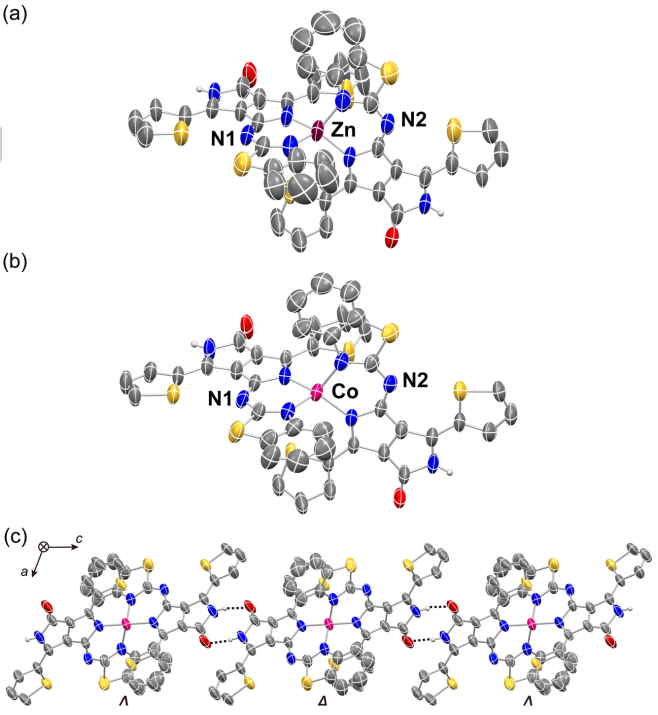

Figure 2. X-ray single crystal structures of (a) **4a** and (b) **5a** and (c) packing diagram of **5a**. Δ Isomers are shown in (a) and (b). The thermal ellipsoids are scaled to 50% probability. Alkoxy substituents and hydrogen atoms except for pyrrolic NHs are omitted for clarity. Dotted lines indicate NH···O hydrogen bonds. N1 and N2 denote the *meso*-nitrogen atoms of the azadipyrrin ligand.

In the UV/vis absorption spectrum, **3b** exhibits a broad absorption at 590 nm with a lower-energy shoulder at 630 nm, whereas the complexes (**4b** and **5b**) show rather intense absorption comprising two bands at 643 and 595 nm for **4b** and 648 and 596 nm for **5b** (Figure 3a). **3b** and **4b** are weakly fluorescent (fluorescence quantum yields: ~0.01 (**3b**) and ~0.02 (**4b**)) (Figures 3b and S10). The smaller Stokes shift of **4b** than that of **3b** indicates a more rigid structure of **4b** due to the metal coordination.

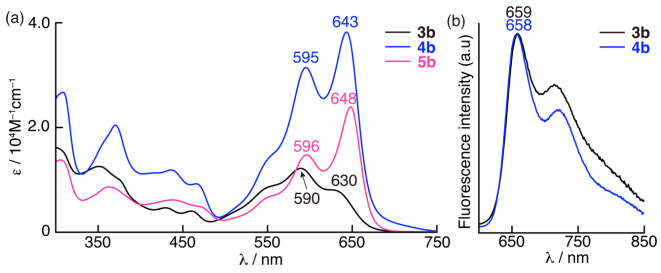

Figure 3. (a) UV/vis absorption spectra of **Janus-PPAD** (**3b**) and its metal complexes (**4b** and **5b**) and (b) fluorescence spectra of **3b** and **4b** in chloroform. The UV/vis absorption spectra were measured at 8.4 × 10^{-5} M for **3b**, 4.4 × 10^{-5} M for **4b**, and 2.9 × 10^{-5} M for **5b**.

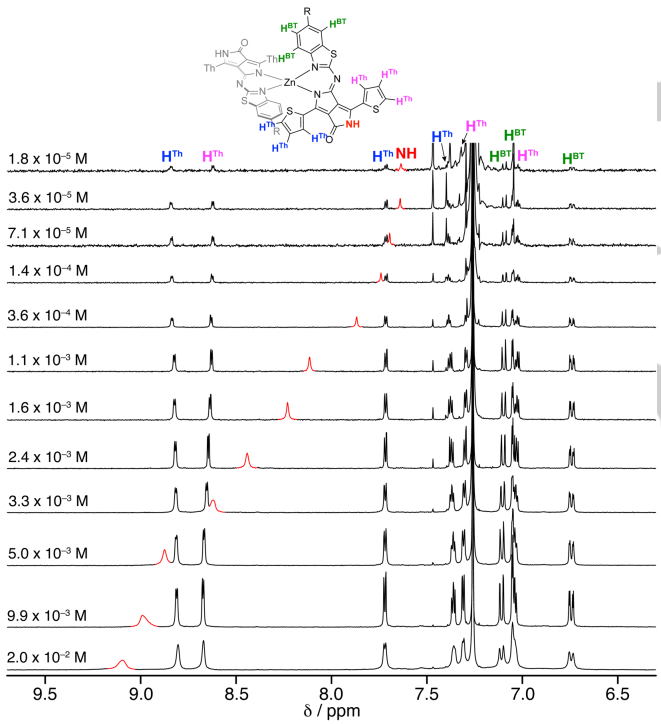

Figure 4. Concentration-dependent ^{1}H NMR spectra of **4b** (1.8 × 10^{-5} M–2.0 × 10^{-2} M) in $CDCl_3$ at 298 K. The NH proton signals are highlighted in red.

To give a detailed insight into the hydrogen-bonding interactions in solution, concentration- and temperature-dependent shifts of the ^{1}H NMR spectra of **4b** were investigated (Figures 4 and S11). As shown in Figure 4, the downfield shifts of the NH proton signal are observed when the concentration is increased from 1.8 × 10^{-5} M to 2.0 × 10^{-2} M (Figure 4). The variable-temperature ^{1}H NMR spectra of a 3.3 mM $CDCl_3$ solution of **4b** also exhibits a similar downfield shift of the NH proton signal from 8.31 ppm at 40 °C to 10.2 ppm at –40 °C together with significant broadening. These results imply the formation of intermolecular hydrogen bonds at high concentration and at low temperature. The concentration-dependent chemical shift of the NH proton was analyzed to estimate the association constant. A smooth sigmoidal curve in the plot of the NH chemical shift as a function of concentration indicates an isodesmic self-assembly process.[12,13] Fitting of the curve to an isodesmic model[13–15] provided an association constant of K = 2.1±0.3 × 10^2 M^{-1} at 25 °C and a degree of polymerization of ca. 2.7 at 2.0 × 10^{-2} M concentration (Figures 5 and S12).

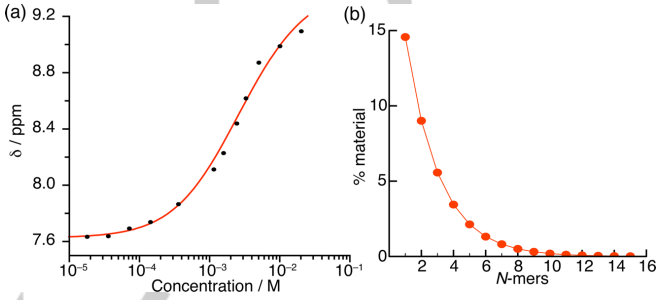

Figure 5. (a) Isodesmic fit of concentration-dependent ^{1}H NMR chemical shifts of the NH proton of **4b** at 298 K in $CDCl_3$. (b) Calculated distribution of *N*-mers at the concentration of 2.0 × 10^{-2} M. See Figure S12 for the detail about the fitting.

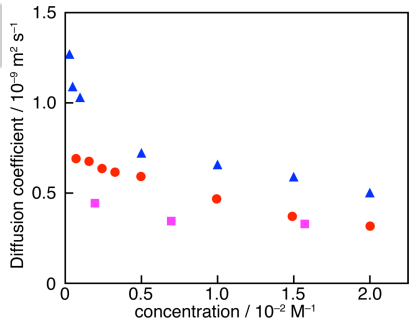

Figure 6. Diffusion coefficients of **4b** (red circle), **7** (pink square), and **8** (blue triangle) at 25 °C in chloroform.

A diffusion coefficient derived from the DOSY spectra is inversely proportional to the size of the molecule or molecular assemblies.[16] At low concentrations, the diffusion coefficients of **4b** and **7** are distributed around a half of those of **8** because the molecular sizes of **4b** and **7** are approximately twice as much as **8** (Figure 6). Despite the similar molecular sizes of **4b** and **7**, the diffusion coefficients of **7** are smaller than those of **4b**. Although the reason is unclear, it is possible that a slight structural difference due to the *N*-methylation may cause certain differences in the diffusion coefficients. Upon increasing concentrations, the diffusion coefficients of **7** slightly decrease to be an almost constant value of ca. 0.3 × 10^{-9} m^2 s^{-1}, whereas those of **4b** and **8** more significantly decrease, reflecting formations of hydrogen-bonded oligomers and a dimer, respectively. The diffusion coefficients of **4b** constantly decrease from the initial value of 0.7 × 10^{-10} m^2 s^{-1} to about half of that upon increasing the concentrations. These results agree with the major distribution of

small oligomer species estimated by the isodesmic fitting analysis on the concentration-dependent chemical shifts of the ^{1}H NMR spectra of **4b** (Figure 5b).

A certain type of tetra-coordinated mono-nuclear cobalt(II) complexes exhibit a large zero-field splitting (zfs) of the ground spin states. Accordingly, this class of complexes are potential candidates for so-called single-molecule magnets (SMMs).[17] Since **Janus-PPAD-Co** has an isolated spin center (i.e., cobalt(II) ion) surrounded by tetrahedrally arranged four coordinating nitrogen atoms, the dynamic magnetic behavior of the spin system and the effect of the intermolecular hydrogen bonds on the magnetic properties are of great interest.

The structural index parameter τ_4' proposed by Okuniewski et al. was evaluated to compare coordination geometries around the cobalt(II) ion for **Janus-PPAD-Co** and some related pseudotetrahedral [CoN_4]-type SMMs.[18] Note that τ_4' values of 1 and 0 represent regular tetrahedral and planar coordination geometry, respectively. Although the τ_4' = 0.81 for **Janus-PPAD-Co** indicates that the coordination geometry is largely distorted from the regular tetrahedron, the deformation is less significant than [Co(half-Pc)$_2$] (0.76)[17c], (HNEt$_3$)$_2$[Co^{II}(L^{2-})$_2$] (0.74)[17d], and [Co{(N*t*Bu)$_3$SMe}$_2$] (0.66)[17e].

The magnetic susceptibility measurements at 1000 Oe revealed that **5a** has the $\chi_M T$ value of 2.21 cm^3 K mol^{-1} at 300 K, indicating that the cobalt has a high-spin d^7 configuration (S = 3/2) with a non-negligible contribution of the spin-orbit coupling (Figure 7a). As the temperature is decreased from 300 K, the $\chi_M T$ gradually declines. The gentle slope until down to about 50 K can be ascribed to the temperature-independent paramagnetism (TIP), while the steeper descent below 50 K to reach 1.33 cm^3 K mol^{-1} at 1.8 K arises from the ligand field splitting.[19] The simulation by employing g_z = 2.12, $g_{x,y}$ = 2.00, D = –27.0 cm^{-1}, and TIP = 8 × 10^{-4} cm^3 mol^{-1} fits well with the experiment (Figure 7a, solid line).

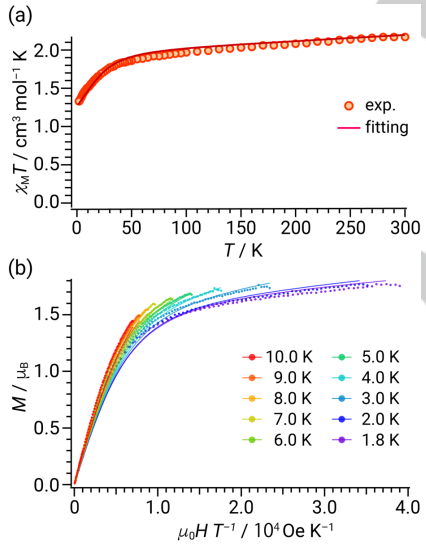

Figure 7. (a) $\chi_M T$ as a function of temperature T for a powder sample of **5a** at an applied field of 1000 Oe. (b) M vs HT^{-1} plot at the indicated temperatures (dots) and the results of the simulations (solid lines).

The *M*-*H* curves show neither hysteresis nor remnant magnetizations even at 1.8 K (Figure S13). The *M*-$\mu_0 HT^{-1}$ plot prepared from the magnetization data at various temperatures is shown in Figure 7b. The dispersion of the collected dots from a single line suggests that the cobalt site of **5a** has a large magnetic anisotropy. The solid lines in Figure 7b are the results of fitting based on the following spin Hamiltonian (1).

$$\hat{H} = g_{\mathrm{iso}}\mu_{\mathrm{B}} S H + D\hat{S}_z^2 + E\left(\hat{S}_x^2 - \hat{S}_y^2\right) \qquad (1)$$

In the fitting, the g value was assumed to be isotropic to reduce the number of parameters. μ_{B} represents the Bohr magneton. D and E are the axial and rhombic zfs parameters, respectively. H, S, and $\hat{S}_x^2$, $\hat{S}_y^2$, and $\hat{S}_z^2$ are magnetic field, spin multiplicity, and spin angular momentum operators, respectively. The best fit was achieved using the following set of parameters: g_{iso}= 2.104, D = −27.1 cm^{-1}, and $|E|$ = 5.17 × 10^{-5} cm^{-1} (Figure 7b, solid lines). The estimated g_{iso} and D values agree well with those obtained from the fitting of the $\chi_M T$ vs T plot. The negative D and small $|E|$ values indicate that the $\langle M_S| = \langle \pm 3/2|$ states are more stable than the $\langle \pm 1/2|$ states; i.e., the complex has an easy-axis magnetic anisotropy.

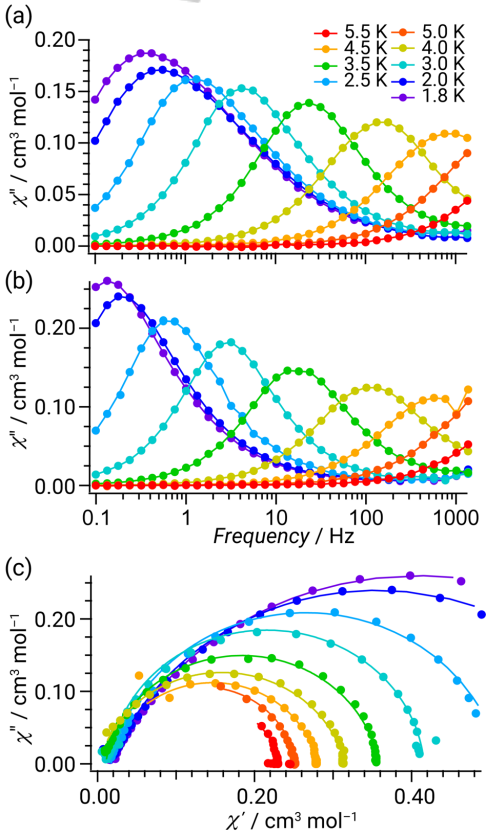

Figure 8. (a, b) Out-of-phase component (χ'') of the ac magnetic susceptibility as a function of ac frequency for (a) **5a** and (b) **dil.5a** at H_{dc} = 1000 Oe. Solid lines are for eye guide. (c) Cole-Cole plots of **dil.5a** at H_{dc} = 1000 Oe. Note that solid lines represent the results of fitting.

Magnetic relaxation properties of **5a** and **5a** diluted with diamagnetic **4a** (**dil.5a**) were examined by ac magnetic susceptibility measurements (See Supporting Information for the detailed preparation procedures for **dil.5a**). The undiluted sample (**5a**) exhibits characteristics of slow magnetic relaxations even in the absence of external static magnetic field (H_{dc}); that is, non-

zero χ'' signals can be recognized around 1000 Hz below 4 K (Figure S14a). The increased average Co–Co distance for **dil.5a** leads to suppression of quantum tunneling magnetization (QTM) driven by the dipole-dipole interactions among the cobalt ions. As shown in Figure S14b, **dil.5a** has additional χ'' signals below 100 Hz, indicating further slowing down of the magnetic relaxation by the dilution. By applying H_{dc} of 1000 Oe, both **5a** and **dil.5a** showed drastic changes in the magnetic relaxation phenomena. Frequency-dependent distinct χ' and χ'' signals below 5 K clearly indicate that the complexes are functioning as the SMMs (Figures 8 and S15).

The semi-circle χ'' vs χ' (Cole-Cole) plots were analyzed based on the generalized Debye model.[20] The results are depicted by solid lines in Figures 8c and S15 and tabulated in Tables S1 and S2. Dispersion coefficients, α, of 0.41 and 0.25 at 1.8 K for **5a** and **dil.5a**, respectively, suggest that more than one substantial magnetic relaxation paths exist in the low temperature range, while smaller α values above 3 K enabled us to fit the Arrhenius plots with a straight line in the high temperature range (Figure S16). The estimated effective energy barriers (U_{eff}) are 38.0 and 37.4 cm^{-1} with the pre-exponential factors (τ_0) of 1.31 × 10^{-9} and 1.84 × 10^{-9} s for **5a** and **dil.5a**, respectively. These results indicate that the Orbach mechanism dominates as the relaxation path in the high temperature range irrespective of the dilution; that is, the $\langle \pm 3/2|$ spin states flip to the $\langle \mp 3/2|$ states, respectively, via the thermally excited $\langle \pm 1/2|$ states. Since the zfs's are less sensitive to the dilution, the estimated U_{eff}'s are approximately identical for **5a** and **dil.5a**.

In contrast, the Arrhenius plots draw different curves in the low temperature range, which can also be recognized by comparing the peak top frequencies below 3 K in Figures 8a and 8b. This implies that some intermolecular interactions that accelerate remaining magnetic relaxations even after applying H_{dc} = 1000 Oe. With lowering the temperature, the thermal excitation from the ground states to the excited $\langle \pm 1/2|$ states is suppressed, and therefore, the Orbach process becomes less significant. As a result, other relaxation mechanisms such as direct, Raman, and QTM processes become prominent. Figure 9 demonstrates the simultaneous fitting of the τ's on the conditions of (a) variable temperatures at a constant H_{dc} of 1000 Oe, and (b) variable H_{dc}'s at 2 K (Figures S17 and S18, and Tables S3 and S4 for original data). The following equation (2) was employed to model the relaxation.[21]

$$\tau^{-1} = AH^5 \coth\left(\frac{g\mu_B H}{2k_B T}\right) + CT^n + \tau_0^{-1}\exp\left(\frac{U_{eff}}{k_B T}\right) + d\frac{1+eH^2}{1+fH^2} \quad (2)$$

In the right-hand side, the direct, Raman, Orbach, and QTM contributions are expressed from left to right, respectively. The A and C are coefficients to be optimized. H represents the applied magnetic field, namely, H_{dc}. The effect of QTM is described by three parameters (d, e, and f). k_B is the Boltzmann constant. The U_{eff} and τ_0 were fixed to the values evaluated in the high temperature range (see above). The best fit was obtained when the following set of parameters was employed: A = 3.0 × 10^2 s^{-1} T^{-5}, C = 1.0 × 10^{-2} s^{-1} K$^{-6.2}$, n = 6.2, d = 55 s^{-1}, e = 0, f = 1.5 × 10^4 T^{-2} (Figure 9). The e parameter in the QTM term represents intermolecular interactions, which is estimated to be zero for **dil.5a**. The n of 6.2 is smaller than that expected for the ideal Kramers system (n = 9), although the range of n varies in practice for coordination compounds.[22] As demonstrated in Figure 9a, the Raman process dominates at H_{dc} = 1000 Oe between 3 K and the lowest temperature, where the contribution of the QTM becomes comparable. The direct process is insignificant under this condition. At 2 K, the Orbach path is negligible, and below 1000 Oe, the magnetic relaxations occur through the QTM mechanism (Figure 9b). In the high H_{dc} range, the direct mechanism dominates (note the fifth power of H factor in the direct term), while the QTM is suppressed according to the denominator of the term. The compensation of two relaxation mechanism results in the maximum relaxation time at ca. 1000 Oe.

Figure S17 compares the χ'' vs frequency plots at various H_{dc}'s below 1000 Oe. The fast component located presumably out of the window shifts to the lower frequency side by the dilution at H_{dc} = 0 in addition to another small peak appearing at ca. 10 Hz. The former gradually disappears with increasing the H_{dc}, while the latter gains intensity. However, the peak frequencies differ between **5a** and **dil.5a** even in the presence of H_{dc} = 1000 Oe, which means the application of the external magnetic field cannot suppress the QTM path perfectly if the Co–Co interactions are present. Although it is often mentioned that the QTM is removed by a magnetic field for SMMs, our results suggest at least some of the QTM paths remain even in the presence of H_{dc} when the spin centers are in proximity.

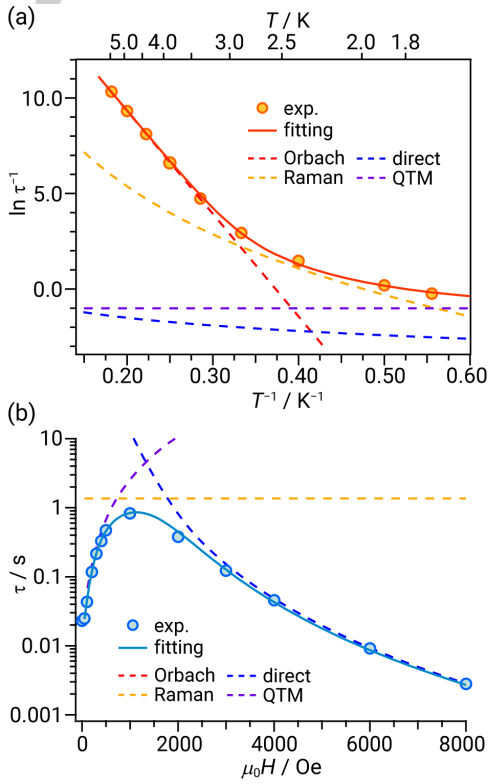

Figure 9. Simultaneous fitting of relaxation times for **dil.5a** using eq. 2 for the conditions of (a) H_{dc} = 1000 Oe and (b) T = 2 K.

Multiconfigurational *ab initio* calculations for **5a** were performed based on the CASSCF model implemented in the ORCA 4.0.1.2 software.[23] The molecular coordinates were modified from the crystal structures (See Supporting Information). The active space was converged at the CAS(7,5) level; that is, seven electrons in the five active 3d-based orbitals. No ligand

orbitals were included. The NEVPT2 calculations for the resultant wave functions were conducted to recover possible dynamic correlations. By including 10 quartets arising from the ^4F and ^4P terms and 35 doublets for a free Co^{II} ion, while the duplicated ^2D term was omitted, magnetic parameters of **5a** have been predicted (Table S5). The estimated negative D value and small rhombicity, $|E/D|$, are consistent with the experiments. The largest contribution to the axial anisotropy is attributed to the first excited quartets; that is the easy axis magnetic anisotropy of **5a** results mainly from the second-order spin-orbit couplings. N1 and N2 nitrogen atoms shown in Figure 2 are approximately on the easy axis. The lowest four wave functions are summarized in Tables S6 and S7. Judging from the weight factors, the mixing of the $\langle M_S| = \langle \pm 3/2|$ states is limited. However, this is the possible reason why the QTM dominates at H_{dc} = 0 even for **dil.5a**. The rapid drop below 50 K in the $\chi_M T$ plots and the dispersion in the M-$\mu_0 H/T$ plot (Figure 7) are rationalized by the large energy gap between the $\langle \pm 3/2|$ and $\langle \pm 1/2|$ states. The ligand field one-electron wave functions of five 3d orbitals were calculated from the AILFT program (Table S8).[24] The two lowest orbitals are fully occupied and have large coefficients for d_{z^2} (-0.934) and d_{xy} (0.994), respectively. The remaining three orbitals are half-filled to give the S = 3/2 ground spin state. The two highest orbitals are described by the linear combinations of the d_{yz} and d_{xz} orbitals, which leads to the unquenched orbital angular momentum contribution to the ground states.

Conclusion

A useful synthetic method to convert one of the lactam units in the structure of DPP to an azadipyrrin ligand was developed, and the orthogonal interactions of **Janus-PPAD** arising from the hydrogen-bonding and metal-coordinating capabilities were investigated. Both cobalt and zinc complexes form hydrogen-bonded one-dimensional arrays in the crystal structures, whereas even in solution, formation of hydrogen-bonded oligomer species was confirmed by concentration- and temperature-dependent ^{1}H NMR and DOSY spectroscopy. In addition to the supramolecular behavior, we have demonstrated that **Janus-PPAD-Co** functions as a SMM in the presence of a static magnetic field. The slow magnetic relaxation occurs based mainly on the Orbach mechanism in the high temperature range, while our results have clarified that the Raman contribution is significant below 3 K. Although the QTM due to the internal origin is efficiently suppressed by applying static magnetic field, that arising from the intermolecular origin remains even in the presence of magnetic field. Considering the Schiff base forming reactions can be applied to other types of bislactam compounds, such as benzodipyrrolidone and isoindigo,[25] we can further extend this study to synthesize various Janus azadipyrrin analogs, in which magnetic interactions can be controlled. The research along this direction will be the future target and reported from our laboratory.

Acknowledgements

This work was supported by Grants-in-Aids for Scientific Research (B) (JSPS KAKENHI Grant Number JP19H02703) and Challenging Exploratory Research (JSPS KAKENHI Grant Number 15H00756).

Keywords: aza-BODIPY • diketopyrrolopyrrole • supramolecular chemistry • coordination chemistry • single-molecule magnet

[1] a) A. Iqbal, M. Jost, R. Kirchmayr, J. Pfenninger, A. Rochat, O. Wallquist, *Bull. Soc. Chim. Belg.* **1988**, *97*, 615–643; b) J. S. Zambounis, Z. Hao, A. Iqbal, *Nature* **1997**, *388*, 131–132; c) Z. M. Hao, A. Iqbal, *Chem. Soc. Rev.* **1997**, *26*, 203–213.

[2] M. Grzybowski, D. T. Gryko, *Adv. Opt. Mater.* **2015**, *3*, 280–320.

[3] M. Kaur, D. H. Choi, *Chem. Soc. Rev.* **2015**, *44*, 58–77.

[4] W. Li, K. H. Hendriks, M. M. Wienk, R. A. J. Janssen, *Acc. Chem. Res.* **2016**, *49*, 78–85.

[5] S. Qu, H. Tian, *Chem. Commun.* **2012**, *48*, 3039–3051.

[6] C. B. Nielsen, M. Turbiez, I. McCulloch, *Adv. Mater.* **2013**, *25*, 1859–1880.

[7] B. Tieke, A. R. Rabindranath, K. Zhang, Y. Zhu, *Beilstein J. Org. Chem.* **2010**, *6*, 830–845.

[8] a) G. M. Fischer, A. P. Ehlers, A. Zumbusch, E. Daltrozzo, *Angew. Chem. Int. Ed.* **2007**, *46*, 3750–3753; *Angew. Chem*. **2007**, *119*, 3824–3827; b) G. M. Fischer, M. Isomäki-Krondahl, I. Göttker-Schnetmann, E. Daltrozzo, A. Zumbusch, *Chem. Eur. J.* **2009**, *15*, 4857–4864; c) G. M. Fischer, E. Daltrozzo, A. Zumbusch, *Angew. Chem. Int. Ed.* **2011**, *50*, 1406–1409; *Angew. Chem*. **2011**, *123*, 1442–1445.

[9] a) K. Skonieczny, I. Papadopoulos, D. Thiel, K. Gutkowski, P. Haines, P. M. McCosker, A. D. Laurent, P. A. Keller, T. Clark, D. Jacquemin, D. M. Guldi, D. T. Gryko, *Angew. Chem. Int. Ed.* **2020**, *59*, 16104–16113; *Angew. Chem*. **2020**, *132*, 16238–16247; b) M. Grzybowski, V. Hugues, M. Blanchard-Desce, D. T. Gryko, *Chem. Eur. J.* **2014**, *20*, 12493–12501; c) M. Grzybowski, E. Glodkowska-Mrowka, T. Stoklosa, D. T. Gryko, *Org. Lett.* **2012**, *14*, 2670–2673.

[10] a) S. Shimizu, *Chem. Commun.* **2019**, *55*, 8722–8743; b) S. Shimizu, T. Iino, Y. Araki, N. Kobayashi, *Chem. Commun.* **2013**, *49*, 1621–1623; c) S. Shimizu, T. Iino, A. Saeki, S. Seki, N. Kobayashi, *Chem. Eur. J.* **2015**, *21*, 2893–2904; d) Y. Kage, H. Karasaki, S. Mori, H. Furuta, S. Shimizu, *ChemPlusChem* **2019**, *84*, 1648–1652.

[11] <url href="<url>https://www.ccdc.cam.ac.uk/services/structures?id=doi:10.1002/chem.202######">Deposition Numbers 2062674 (for **4a**) and 2062675 (for **5a**) </url> contains the supplementary crystallographic data for this paper. These data are provided free of charge by the joint Cambridge Crystallographic Data Centre and Fachinformationszentrum Karlsruhe Access Structures service <url href="https://www.ccdc.cam.ac.uk/structures/?">www.ccdc.cam.ac.uk/structures</url>.

[12] T. F. A. De Greef, M. M. J. Smulders, M. Wolffs, A. P. H. J. Schenning, R. P. Sijbesma, E. W. Meijer, *Chem. Rev.* **2009**, *109*, 5687–5754.

[13] Z. Chen, A. Lohr, C. R. Saha-Möller, F. Würthner, *Chem. Soc. Rev.* **2009**, *38*, 564–584.

[14] M. M. J. Smulders, M. M. L. Nieuwenhuizen, T. F. A. de Greef, P. van der Schoot, A. P. H. J. Schenning, E. W. Meijer, *Chem. Eur. J.* **2010**, *16*, 362–367.

[15] N. Ponnuswamy, G. D. Pantoş, M. M. J. Smulders, J. K. M. Sanders, *J. Am. Chem. Soc.* **2012**, *134*, 566–573.

[16] Y. Cohen, L. Avram, L. Frish, *Angew. Chem. Int. Ed.* **2005**, *44*, 520–554; *Angew. Chem.* **2005**, *117*, 524–560.

[17] a) J. M. Zadrozny, J. R. Long, *J. Am. Chem. Soc.* **2011**, *133*, 20732–20734; b) M. S. Fataftah, J. M. Zadrozny, D. M. Rogers, D. E. Freedman, *Inorg. Chem.* **2014**, *53*, 10716–10721; c) T. Ishizaki, T. Fukuda, M. Akaki, A. Fuyuhiro, M. Hagiwara, N. Ishikawa, *Inorg. Chem.* **2019**, *58*, 5211–5220; d) Y. Rechkemmer, F. D. Breitgoff, M. van der Meer, M. Atanasov, M. Hakl, M. Orlita, P. Neugebauer, F. Neese, B. Sarkar, J. van Slageren, *Nat. Commun.* **2016**, *7*, 10467–10474; e) E. Carl, S. Demeshko, F. Meyer, D. Stalke, *Chem. Eur. J.* **2015**, *21*, 10109–10115.

[18] A. Okuniewski, D. Rosiak, J. Chojnacki, B. Becker, *Polyhedron* **2015**, *90*, 47–57.

[19] a) S. Ziegenbalg, D. Hornig, H. Görls, W. Plass, *Inorg. Chem.* **2016**, *55*, 4047−4058; b) R. Boča, C. Rajnák, J. Moncol, J. Titiš, D. Valigura, *Inorg. Chem.* **2018**, *57*, 14314−14321; c) R. Mitsuhashi, S. Hosoya, T. Suzuki,

Y. Sunatsuki, H. Sakiyama, M. Mikuriya, *Dalton Trans.* **2019**, *48*, 395–399.

[20] a) K. S. Cole, *J. Chem. Phys.* **1941**, *9*, 341–351; b) C. Dekker, A. F. M. Arts, H. W. de Wijn, A. J. van Duyneveldt, J. A. Mydosh, *Phys. Rev. B* **1989**, *40*, 11243–11251; c) S. M. J. Aubin, Z. Sun, L. Pardi, J. Krzystek, K. Folting, L.-C. Brunel, A. L. Rheingold, G. Christou, D. N. Hendrickson, *Inorg. Chem.* **1999**, *38*, 5329–5340.

[21] a) A. C. De Vroomen, E. E. Lijphart, N. J. Poulis, *Physica* **1970**, *47*, 458–484; b) A. Abragam, B. Bleaney, Electron Paramagnetic Resonance of Transition Ions, Clarendon, Oxford, **1970**; c) M. Atzori, L. Tesi, S. Benci, A. Lunghi, R. Righini, A. Taschin, R. Torre, L. Sorace, R. Sessoli, *J. Am. Chem. Soc.* **2017**, *139*, 4338−4341.

[22] a) A. Singh, K. N. Shrivastava, *Phys. Status Solidi B* **1979**, *95*, 273−277; b) K. N. Shriyastava, *Phys. Status Solidi B* **1983**, *117*, 437–458.

[23] a) E. A. Suturina, D. Maganas, E. Bill, M. Atanasov, F. Neese, *Inorg. Chem.* **2015**, *54*, 9948−9961; b) V. G. Chilkuri, S. DeBeer, F. Neese, *Inorg. Chem.* **2017**, *56*, 10418−10436.

[24] a) L. Rigamonti, N. Bridonneau, G. Poneti, L. Tesi, L. Sorace, D. Pinkowicz, J. Jover, E. Ruiz, R. Sessoli, A. Cornia, *Chem. Eur. J.* **2018**, *24*, 8857–8868; b) M. K. Thomsen, A. Nyvang, J. P. S. Walsh, P. C. Bunting, J. R. Long, F. Neese, M. Atanasov, A. Genoni, J. Overgaard, *Inorg. Chem.* **2019**, *58*, 3211−3218.

[25] M. Tamada, T. Iino, Y. Wang, M. Ide, A. Saeki, H. Furuta, N. Kobayashi, S. Shimizu, *Tetrahedron Lett.* **2017**, *58*, 3151–3154.

Entry for the Table of Contents

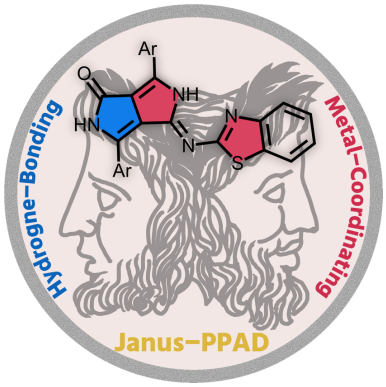

Janus pyrrolopyrrole azadipyrrin (**Janus-PPAD**) with a Janus duality resulting from the hydrogen-bonding ketopyrrole and metal-coordinating azadipyrrin moieties was synthesized by a Schiff base forming reaction of diketopyrrolopyrrole and azaarylamine. In addition to the self-complementary assembly, the cobalt complex functions as a single-molecule magnet in the presence of static magnetic field.